ACS NANO
Cite This: ACS Nano 2019, 13, 12042−12051
www.acsnano.org

ARTICLE

High-Performance Transparent Ultraviolet Photodetectors Based on InGaZnO Superlattice Nanowire Arrays

Fangzhou Li,[†] You Meng,[†] Ruoting Dong,[†] SenPo Yip,[†,‡,§] Changyong Lan,[⊥] Xiaolin Kang,[†] Fengyun Wang,[#] Kwok Sum Chan,[§,∥] and Johnny C. Ho*[,†,‡,§]

[†]Department of Materials Science and Engineering, City University of Hong Kong, Kowloon, Hong Kong
[‡]State Key Laboratory of Terahertz and Millimeter Waves, City University of Hong Kong, Kowloon, Hong Kong
[§]Centre for Functional Photonics, City University of Hong Kong, Kowloon, Hong Kong
[⊥]School of Optoelectronic Science and Engineering, University of Electronic Science and Technology of China, Chengdu 610054, China
[#]College of Physics and State Key Laboratory of Bio-Fibers and Eco-Textiles, Qingdao University, Qingdao 266071, China
[∥]Department of Physics, City University of Hong Kong, Kowloon Tong, Hong Kong

Supporting Information

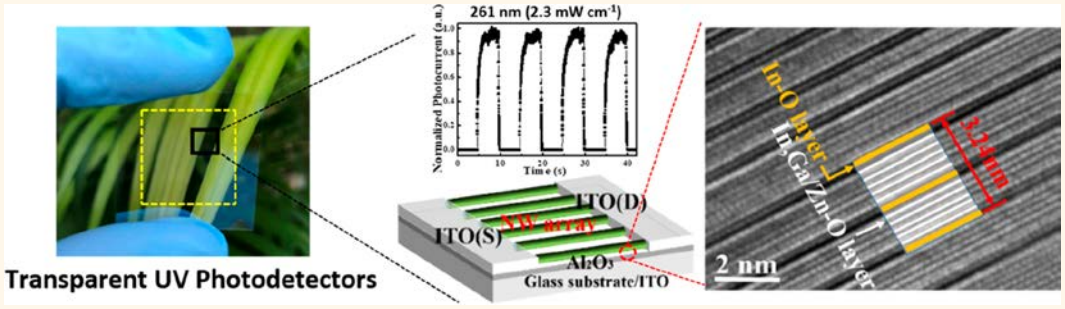

ABSTRACT: Due to the efficient photocarrier separation and collection coming from their distinctive band structures, superlattice nanowires (NWs) have great potential as active materials for high-performance optoelectronic devices. In this work, InGaZnO NWs with superlattice structure and controllable stoichiometry are obtained by ambient-pressure chemical vapor deposition. Along the NW axial direction, perfect alternately stacking of $InGaO(ZnO)_4^+$ blocks and InO_2^- layers is observed to form a periodic layered structure. Strikingly, when configured into individual NW photodetectors, the Ga concentration is found to significantly influence the amount of oxygen vacancies and oxygen molecules adsorbed on the NW surface, which dictate the photoconducting properties of the NW channels. Based on the optimized Ga concentration (*i.e.*, $In_{1.8}Ga_{1.8}Zn_{2.4}O_7$), the individual NW device exhibits an excellent responsivity of 1.95×10^5 A/W and external quantum efficiency of as high as 9.28×10^7% together with a rise time of 0.93 s and a decay time of 0.2 s for the ultraviolet (UV) photodetection. Besides, the obtained NWs can be fabricated into large-scale parallel arrays on glass substrates as well to achieve fully transparent UV photodetectors, where the performance is on the same level or even better than many transparent photodetectors with high performance. All the results discussed above demonstrate the great potential of InGaZnO superlattice NWs for next-generation advanced optoelectronic devices.

KEYWORDS: *transparent, ultraviolet photodetectors, superlattice, InGaZnO, nanowires*

In the past decade, due to many fascinating properties, great attention has been paid to one-dimensional (1D) inorganic semiconductor nanowires (NWs) for various device applications in transistors, gas sensors, photodetectors, light-emitting diodes, solar cells, *etc.*[1−6] In particular, UV photodetectors based on the binary metal oxide NWs, such as In_2O_3, Ga_2O_3, and ZnO, are demonstrated with impressive device performances in higher responsivity, faster response time, better external quantum efficiency (EQE), and greater carrier mobility as compared with those of the bulk or thin-film materials based counterparts.[7−10] These UV detectors would have particular utilization in tracking missiles, flame detection,

Received: August 9, 2019
Accepted: October 3, 2019
Published: October 3, 2019

DOI: 10.1021/acsnano.9b06311
ACS Nano 2019, 13, 12042−12051

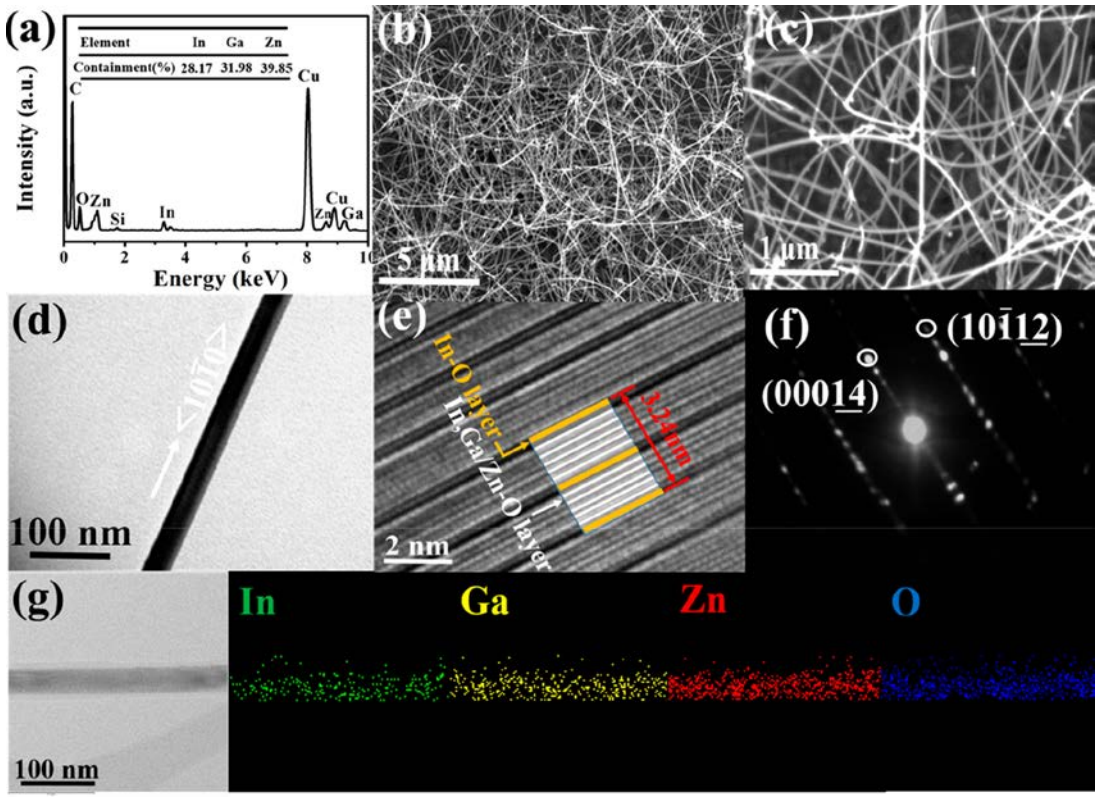

Figure 1. (a) EDS, (b, c) SEM, (d) TEM, (e, f) HRTEM image and SAED pattern of typical $In_{1.8}Ga_{1.8}Zn_{2.4}O_7$ NWs. (g) STEM image of a representative $In_{1.8}Ga_{1.8}Zn_{2.4}O_7$ NW with the elemental mapping of In, Ga, Zn, and O, respectively.

and many others.[7−10] Apart from the binary oxides, ternary and even multielement metal oxide NW material systems are even recently observed to have a wider tunability range of physical properties for further device performance enhancement; however, because of the challenge of material synthesis, there are only a few reports investigating these ternary and multielement NWs for photodetection.[11−15] In principle, these photodetectors can also be made into optically transparent solar-blind devices, where they would have a boarder range of potential applications in smart windows, optical communications, security, human motion detection, and many others.[16−20] In this regard, it is important to fabricate high-quality multielement metal oxide NWs together with the careful assessment of their corresponding photodetection mechanisms and performance limits as transparent photodetectors, in which all these would contribute to a substantial advancement of semiconductor NWs for next-generation high-performance optoelectronics.

At the same time, these InGaZnO crystalline NWs with superlattice structure have been lately achieved for high-mobility thin-film transistors.[21,22] The optimal Ga concentration and the superlattice structure are likely to tune the carrier concentration and at the same time reduce the concentration of oxygen vacancies to improve the property of the NW transistor.[23] In general, superlattice NWs are highly preferred as active channel materials for photodetectors due to their distinctive band structures and band alignments such that a more efficient photocarrier separation and collection result.[24,21] Upon illumination, the photoexcited electrons and holes are spatially separated at the heterointerfaces within the superlattice NWs; therefore, the carrier recombination can be greatly suppressed to increase the EQE value and the spectral responsivity of the NW devices.[25] For instance, Shen *et al.* focused on individual $InGaO_3(ZnO)$ superlattice NWs for flexible ultraviolet (UV) photodetectors with an emphasis on device mechanical robustness, but their device performances, especially the photoresponsivity and on−off current ratio, are still insufficient for advanced utilizations.[25] Until now, to the best of our knowledge, there is not any other work systematically evaluating the optoelectronic properties of InGaZnO superlattice NWs.

In this work, we have successfully fabricated high-performance transparent UV photodetectors utilizing crystalline InGaZnO NW arrayed channels with superlattice structure and well-controlled stoichiometry. Specifically, these NWs exhibit a periodic layered structure with perfect alternately stacking of $InGaO(ZnO)_4^+$ blocks and InO_2^- layers oriented along the NW axial direction. Strikingly, when configured into individual NW photodetectors, the Ga concentration is found to significantly dictate the photoconducting properties of the NW channels. The InGaZnO NWs with an optimal Ga concentration (*i.e.*, $In_{1.8}Ga_{1.8}Zn_{2.4}O_7$) can deliver a good photoresponsivity of up to 1.95×10^5 A/W, an EQE approaching 9.28×10^7%, an on−off current ratio of 1.9×10^5, and rise time and decay times of down to 0.93 and 0.2 s, respectively; these performance parameters are already on the same level or even better than many advanced one-dimensional nanomaterials-based UV photodetectors. These impressive device characteristics are mainly attributed to the reduced density of oxygen vacancies as well as the excellent crystallinity of obtained superlattice NWs. Besides, these NWs can also be fabricated into large-scale parallel arrays on glass substrates to achieve fully transparent UV photodetectors. The results discussed above demonstrate the great potential of InGaZnO

DOI: 10.1021/acsnano.9b06311
ACS Nano 2019, 13, 12042−12051

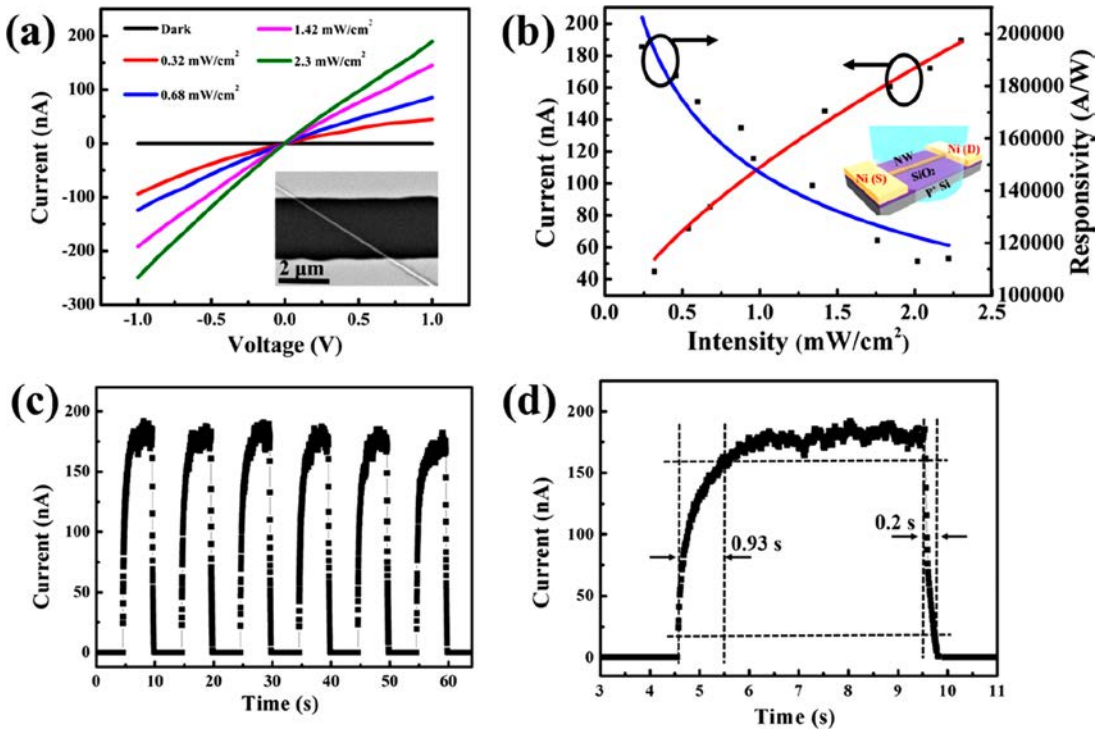

Figure 2. Photoresponse characteristics of the $In_{1.8}Ga_{1.8}Zn_{2.4}O_7$ NW device. (a) *I*–*V* results of the device measured under different power intensities of 261 nm light illumination and in the dark. The inset shows the SEM image of the photodetector. (b) Dependence of photocurrent and responsivity on the light intensity. The inset depicts the illustrative device schematic of the NW photodetector. (c) Current *versus* time curve measured under a light intensity of 2.3 mW/cm². (d) Corresponding high-resolution current *versus* time curve. The bias is 1 V and V_g = −20 V.

NWs with superlattice structure for the future advanced optoelectronic devices.

RESULTS AND DISCUSSION

After the NWs are synthesized, energy dispersive X-ray spectrometry (EDS) measurement is performed on the obtained NWs. As shown in the EDS spectrum in Figure 1a and Supporting Information Figure S1, the corresponding metallic composition of the NWs are evaluated. Moreover, X-ray diffraction (XRD) measurement is also carried out to assess the crystal structure of the NWs. We can see that all peaks of InGaZnO NWs can be determined to be $InGaZn_4O_7$ (PDF No. 40-0254) with hexagonal structure and diffraction peaks of IZO NWs belong to $Zn_4In_2O_7$ (PDF No. 20-1438) (Supporting Information Figure S2). Except for the peaks of ZnO (110) and Si (200), which are also observed in other reports,[26,27] there are no other impurity phases witnessed, suggesting that both IGZO and IZO NWs have been fabricated successfully here. By combining EDS and XRD spectrum, the NW samples can be determined to be $In_{1.8}Ga_{1.8}Zn_{2.4}O_7$, $Zn_4In_2O_7$, $In_{2.4}Ga_{0.3}Zn_{3.3}O_7$, and $In_{0.3}Ga_{3.9}Zn_{1.8}O_7$ (Figure 1a and Supporting Information Figures S3 to S5), by just tuning the amount of Ga in the source, respectively. In order to show the repeatability of the NW samples, all of the obtained NWs have been fabricated at least five times repeatedly with the variation within 3 at. % (Figure S6), indicating the stability of this growth method. Importantly, all NW samples exhibit a uniform diameter with a smooth surface and tens of micrometers in the length. Specifically, the average diameter of $In_{1.8}Ga_{1.8}Zn_{2.4}O_7$ NWs is 26 ± 12 nm (Figure 1b). The high-resolution scanning electron microscopy (SEM) image even reveals that small particles appeared at the end of the NWs, which suggests the growth of InGaZnO NWs following the vapor–liquid–solid (VLS) growth mechanism (Figure 1c).[28−30] As expected, the TEM image as well shows a perfectly smooth NW surface and a dominant growth orientation of the NW consistent with the XRD results discussed above (Figure 1d). More importantly, when high-resolution transmission electron microscopy (HRTEM) measurement is conducted, layered structures containing dark and bright stripes can be seen for the InGaZnO NW (Figure 1e), elucidating the formation of a NW superlattice structure.[31] In particular, every five thin dark lines (In,Ga/Zn–O layers) are coupled by two thick dark lines (In–O layers), confirming the superlattice structure of IGZO NWs.[32] Indeed, when selected area electron diffraction (SAED) information is collected (Figure 1f), the pattern of the diffraction spot exhibits features of the superlattice structure.[33] Explicitly, between every two main spots exists five satellite spots, which is also in good agreement with the XRD result shown in Supporting Figure S2. It is also noted that all other NW samples exhibit the superlattice structure, while the lattice constant (*c*, two times the distance between two adjacent In–O layers) of the NWs is found to be reduced with increasing Ga concentration (Figure 1e, Supporting Information Figures S3e, S4e, and S5e). This lattice shrinkage is somewhat to be predicted since In can be replaced by Ga, which has a smaller ion radius; therefore, the *c* parameter values are decreased accordingly when more Ga is incorporated into the lattice.[33] Besides, scanning TEM (STEM) equipped with elemental mappings illustrate the uniform distribution of constituent elements of the InGaZnO NW (Figure 1g). Similar results can as well be observed for other NWs in Supporting Information Figures S3g, S4g, and S5g. All these findings confirm the

DOI: 10.1021/acsnano.9b06311
ACS Nano 2019, 13, 12042−12051

Table 1. Comparison of the Characteristic Parameters of the IGZO Nanowire Photodetector with Other Nanoscale Photodetectors

1D photodetector	responsivity/A/W	EQE/%	on−off ratio	rise time/s	decay time/s	ref
ZnO nanowire			800	0.7	0.5	35
$ZnGa_2O_4$ nanowire	3174	1.1×10^6	120	15	10	11
Ga_2O_3 nanowire	33.7	1.67×10^4	400	11.8	<0.3	36
ZnO nanowire			1000	40	300	37
ZnO nanorod			80−85	>500	∼500	38
SnO_2-coated ZnO nanowire			5.5	1.5	25.6	39
ZnO nanowire			180	43.7		40
Ga_2O_3 nanobelt	32	1.59×10^4	100	2.4	<0.6	7
Cu-doped ZnO nanobelt	400	1.7×10^5	∼100	9	17	41
IGZO nanowire	1.95×10^5	9.28×10^7	1.93×10^5	0.93	0.2	this work

realization of high-quality InGaZnO NWs with controllable chemical composition investigated here.

To shed light onto the optoelectronic properties of obtained InGaZnO NWs, photodetectors made of individual NWs are first fabricated and characterized under UV illumination. As shown in the illustrative device schematic in Figure 2b inset, the photodetector consists of an $In_{1.8}Ga_{1.8}Zn_{2.4}O_7$ NW configured onto the surface of Si/SiO_2 as the active channel with Ni electrodes on both ends. The Figure 2a inset gives the typical top-view SEM image of the device, while Figure 2a displays the corresponding current−voltage (I−V) characteristics measured under various power intensities (0.32−2.3 mW cm^{-2}) of 261 nm light irradiation and in the dark, respectively. Although there is a possibility of the oxidation of Ni at the interface when using Ni as the electrodes, the linear relationship exhibited in the I−V curve (Figure 2a) suggests the ohmic-like contact behavior of the photodetector device, which favors the photogenerated carrier collection. In this way, the Ni oxidation effect can be neglected here. In fact, Ni electrodes are widely employed in many other metal oxide NW devices.[23] When the illumination intensity increases, the output current increases accordingly, indicating the effective photoresponse of the device. In order to further evaluate its photoresponse performance, the relationship between the photocurrent (difference between output current under light and in the dark) and the intensity of light is assessed and compiled in Figure 2b. Its relationship can be well described by the power law

$$I_p = AP^{\theta} \tag{1}$$

where I_p is the photocurrent, A is a constant, P is the light intensity, and θ is the empirical value. By the fitting process, the value of θ is estimated to be 0.65, revealing the sublinear relationship between photocurrent and light intensity, which is often observed in metal-oxide-based photoconductors because of the complex processes of electron−hole generation, trapping, and recombination in the semiconductors.[3,34] In addition, responsivity (R) and EQE are two important parameters to appraise the sensitivity of a photodetector, in which they are defined as

$$R = I_p/(PS) \tag{2}$$

$$\mathrm{EQE} = (hc/e\lambda)R \tag{3}$$

where S is the irradiated area of the photodetector, h is Planck's constant, λ is the illumination wavelength, e is the electronic charge, and c is the velocity of light. As given in Figure 2b, R is observed to decrease gradually with increasing illumination intensity. At the voltage of 1 V and the light intensity of 2.3 mW cm^{-2}, the value of R and its corresponding EQE are found to be 1.95×10^5 A/W and 9.28×10^7%, accordingly. Such results show the excellent sensitivity of our devices for UV photodetection.

Furthermore, reproducibility and response speed are another two important figures-of-merit of the photodetectors. Figure 2c describes the transient photoresponse measurement of the photodetector by chopping the light repeatedly. It is obvious that the device yields an impressive on−off current ratio of around 1.9×10^5, and there is no significant change of the on- and off-current among the measurement cycles, indicating a good reproducibility and stability of the device. A high-resolution current *versus* time curve is then used to study the response time of the device. Usually, the rise time and decay time are defined as the peak value of the photocurrent changing from 10% to 90% and 90% to 10%, respectively. In this case, the rise time and decay time are measured to be 0.93 and 0.2 s, accordingly, as illustrated in Figure 2d. At the same time, $Zn_4In_2O_7$, $In_{2.4}Ga_{0.3}Zn_{3.3}O_7$, and $In_{0.3}Ga_{3.9}Zn_{1.8}O_7$ NWs are also configured into photodetectors with the exact same device structure and then characterized, correspondingly (Supporting Information Figures S8 to S10). The device performance of the $In_{1.8}Ga_{1.8}Zn_{2.4}O_7$ NW photodetector is witnessed to be the best among all other samples. When compared with other state-of-the-art one-dimensional nanomaterials based UV photodetectors, the performance parameters of the $In_{1.8}Ga_{1.8}Zn_{2.4}O_7$NW device are already comparable or even better than those reported in the literature, which demonstrates the excellent prospect of our InGaZnO NWs for highly efficient UV photodetection.

Typically, oxygen adsorption and desorption processes are always considered to be closely related to the carrier recombination dynamics of metal-oxide-based photodetectors.[42−44] Here, to further clarify the principle of photoconduction of InGaZnO NW devices, a proposal of the photoconduction mechanism is reinforced in Figure 3. In the dark environment, there would be a large amount of ambient oxygen molecules adsorbed onto the NW channel surface, in which these molecules capture surface free electrons to become O_2^-; therefore, a depletion layer results on the NW surface to yield the low conductivity (Figure 3a). This depletion layer would then induce a band bending near the NW surface (Figure 3b). In this case, when the device is illuminated under UV light irradiation, electron−hole pairs are generated while the photoexcited holes roll to the NW surface to recombine with the ionized oxygen molecules due to the band bending (Figure 3c). During this process, the previously adsorbed

DOI: 10.1021/acsnano.9b06311
ACS Nano 2019, 13, 12042−12051

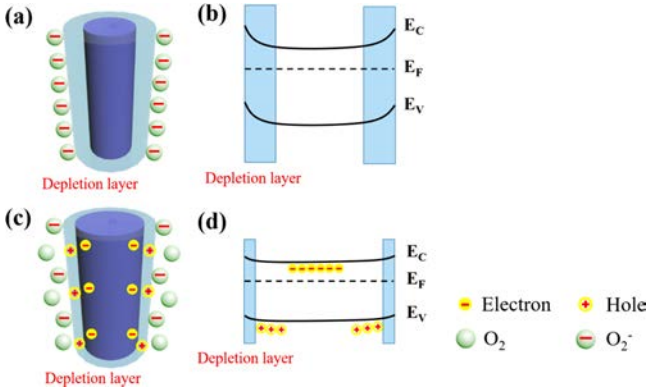

Figure 3. (a, c) Schematic of the InGaZnO NWs along with the interaction with their ambient environment and (b, d) their corresponding energy band diagrams exposed in the dark and under UV illumination.

oxygen molecules are now released and the holes are trapped on the NW surface, leading to the thickness reduction of the surface depletion layer. In this way, the surface band bending of the NW is lessened such that the conductivity would get recovered (Figure 3d). However, after the UV illumination is chopped off, the oxygen molecules are then readsorbed back onto the NW surface again, returning to the original state. Vacuum measurement of the device is purposely performed to validate the proposed photoconduction mechanism as discussed above (Supporting Information Figure S7).

Apart from the interaction with the ambient environment, it is also important to study the property of photodetectors of these NWs with different compositions, especially with different Ga concentrations. In this case, the performance data of different NW devices are extracted from Supporting Information Figures S8 to S10 and presented in Figure 4. It is clear that with the increasing of Ga concentration, the dark current exhibits a reducing trend for the photodetector devices, which significantly drops from 133 nA to 2.3×10^{-5} nA with a source−drain bias of 1 V and gate bias of −20 V (Figure 4a). Meanwhile, both the rise time and decay time deliver the same decreasing characteristics down to 0.91 and 0.07 s, respectively, with the increasing Ga concentration (Figure 4b). It can be understood that the increase of Ga content would possibly lead to the reduction of free electron generation due to the higher bonding energy of Ga−O such that the amount of oxygen vacancies and oxygen adsorption is restrained.[45,46] As we discussed above, the oxygen adsorption on the NW surface can significantly affect its photodetection property. When the oxygen molecules are adsorbed onto the surface of NWs, they can capture free electrons and turn into O_2^-, subsequently decreasing the dark current of the device. Besides, the oxygen adsorption is also responsible for the slow response time.[47,48] In this case, the higher Ga concentration can effectively suppress the oxygen adsorption on the NW surface, induce less ionized oxygen molecules, and then lead to a faster response time. In contrast, the responsivity is observed to first decrease slightly from 7.15×10^4 A/W to 6.64×10^4 A/W, then significantly increase to 1.95×10^5 A/W, and finally drop to 1520 A/W (Figure 4c). EQE shares the same trend as that of the responsivity, starting from 3.4×10^7% to 3.16×10^7%, then increase to 9.28×10^7% and finally reach 7.2×10^5% (Figure 4d). Typically, the photocurrent is proportional to the carrier mobility and the carrier lifetime,[49] while the carrier lifetime is heavily dictated by the density of recombination centers. As a result, as the mobility of A2 is just slightly larger than that of A1,[23] they deliver similar photodetection performance here; however, the device performance can be greatly improved (or deteriorated) if the carrier mobility is largely enhanced for the sample of A3 (or decreased for the sample of A4). All these results clearly illustrate that the Ga concentration of InGaZnO NWs can substantially affect the property of photodetectors with the optimal Ga content for the superior photodetection characteristics.

Furthermore, X-ray photoelectron spectroscopy (XPS) studies are also carried out to evaluate the chemical state of NW constituents as well as to further illustrate the influence of Ga content on their photoconduction property of devices. It is obvious that only In, Ga, Zn, O, and C peaks (from the air) are

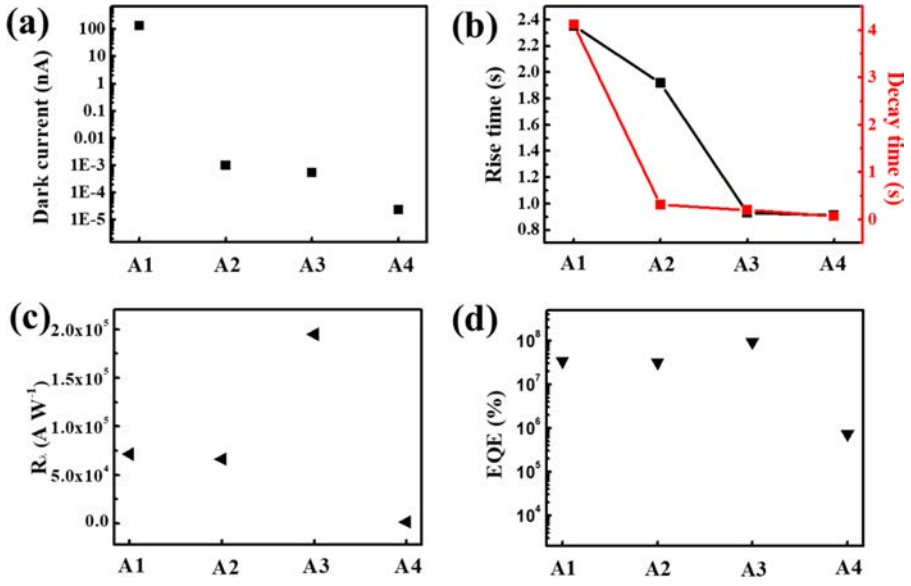

Figure 4. Compiled performance data of four NW devices. (a) Dark current, (b) response time, (c) responsibility, and (d) EQE. The bias is 1 V and V_g = −20 V (A1: $Zn_4In_2O_7$; A2: $In_{2.4}Ga_{0.3}Zn_{3.3}O_7$; A3: $In_{1.8}Ga_{1.8}Zn_{2.4}O_7$; A4: $In_{0.3}Ga_{3.9}Zn_{1.8}O_7$).

DOI: 10.1021/acsnano.9b06311
ACS Nano 2019, 13, 12042−12051

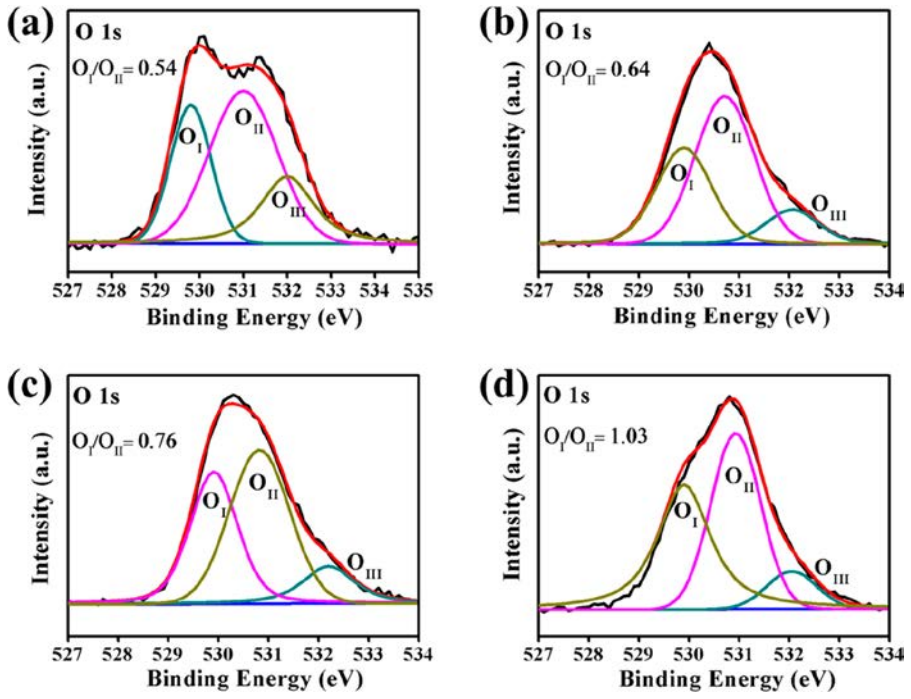

Figure 5. XPS of the deconvoluted O 1s profiles of (a) $Zn_4In_2O_7$, (b) $In_{2.4}Ga_{0.3}Zn_{3.3}O_7$, (c) $In_{1.8}Ga_{1.8}Zn_{2.4}O_7$, and (d) $In_{0.3}Ga_{3.9}Zn_{1.8}O_7$ NWs, respectively.

detected, which confirms again the successful fabrication of both InZnO and InGaZnO NWs (Figure S11). When the high-resolution XPS spectra of both Zn 2p 3/2 and In 3d are inspected, the peaks of Zn 2p 3/2 and In 3d of InGaZnO NWs are slightly red-shifted compared with the peak position of IZO NWs, where this shift is probably coming from the smaller diameter of InGaZnO NWs and the size effect as reported in previous works (Supporting Information Figure S11b and c).[50,51] Notably, the O 1s spectra of all NW samples consist of three kinds of oxygen levels, as depicted in Figure 5.[52] In general, the small binding energy (~529.8 eV) peak, labeled as O_I, is always related to the O^{2-} ions from the substitutional site of InZnO or InGaZnO lattice. The binding energy around 530.9 eV labeled as O_{II} belongs to oxygen vacancies existing in the lattice. The binding energy around 532.5 eV of O_{III} is ascribed to the oxygen species (*e.g.*, H_2O, $-CO_3$) or other species weakly bonded on the NW surface.[53,54] Usually, the area ratio of O_I/O_{II} is employed to demonstrate the relative concentration of oxygen vacancies, which can generate carriers within the lattice of the materials.[55] The ratio values are determined to be 0.54, 0.64, 0.76, and 1.03 for $Zn_4In_2O_7$, $In_{2.4}Ga_{0.3}Zn_{3.3}O_7$, $In_{1.8}Ga_{1.8}Zn_{2.4}O_7$, and $In_{0.3}Ga_{3.9}Zn_{1.8}O_7$ NWs, respectively. The variation of the peak area ratio (*i.e.*, percentage) of O_I, O_{II}, and O_{III} peaks of all NW samples is also compiled in Supporting Information Figure S12 in order to better demonstrate the change of the O 1s peaks. This result indicates that the reduction of oxygen vacancies can be achieved here by incorporating Ga atoms and increasing their concentration in the superlattice NW due to the stronger bonding of Ga−O. It is noted that the higher bonding energy of Ga−O can also lead to a lower formation of oxygen vacancies, which subsequently suppress the generation of free carriers and induce a lower concentration of O_2^- adsorbed on the NW surface.[56] In this way, the lower free electron concentration of the sample can result in a lower dark current, while the adsorbed oxygen molecules are responsible for the slow process of the photoconductivity performance.[57] Therefore, increasing the Ga content here can reduce the dark current and improve the response speed of the optoelectronic devices. More importantly, suppressing the generation of oxygen vacancies can diminish the carrier scattering, thereby improving the mobility and enhancing the responsivity of the superlattice device.[58] Anyhow, when the Ga concentration is too high, the excess Ga species can partly destroy the lattice structure and then degrade the device performance. In this case, the suitable Ga concentration within the InGaZnO NWs can deliver the highest responsivity and EQE value for the photodetectors, as described in Figure 4c and d.

For practical applications, it is essential to evaluate the device performance of photodetectors based on large-scale NW parallel arrays. In this work, $In_{1.8}Ga_{1.8}Zn_{2.4}O_7$ NWs are chosen as the active materials for the construction of parallel arrayed devices because of their enhanced photodetection properties as discussed above. By using the well-established NW contact printing, NW parallel arrays can be readily configured onto any substrate, such as Si/SiO_2 wafers, with the source−drain electrical contact of Ni films (Supporting Information S13a and b insets).[59−61] Supporting Information Figure S13a illustrates the typical $I-V$ characteristics of the fabricated photodetector in the dark as well as under different light intensities (0.18−0.6 mW/cm^2), respectively. With increasing intensity, the output current increases accordingly. The device also exhibits a characteristic linear relationship of $I-V$ curves, indicating the ohmic-like contact property, which favors collecting the photogenerated carriers efficiently. As shown in the curves of photocurrent and responsivity *versus* light intensity (Supporting Information Figure 13b), the relationship between the photocurrent and the light intensity can as well be described by the power law. The θ value is determined to be 0.62, which is again less than 1, suggesting the complex processes of electron−hole generation, trapping, and recombination on the NW surface. Besides, the

DOI: 10.1021/acsnano.9b06311
ACS Nano 2019, 13, 12042−12051

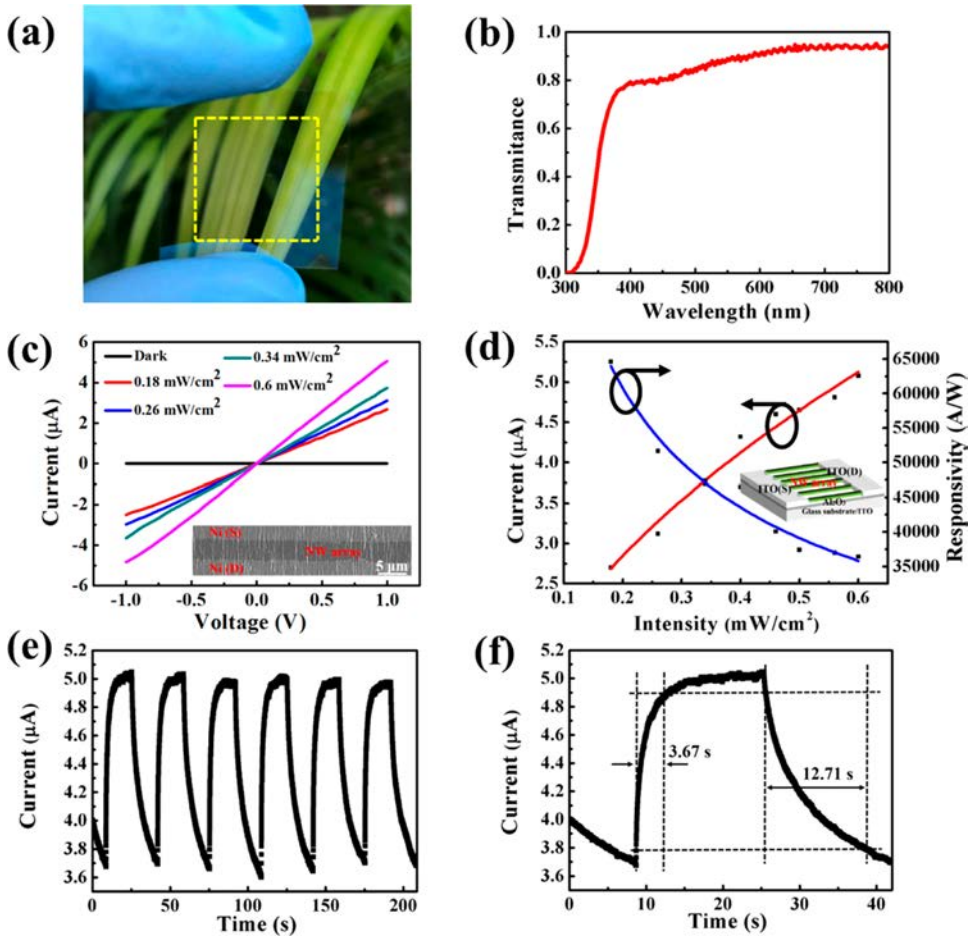

Figure 6. Transparent photodetector device based on $In_{1.8}Ga_{1.8}Zn_{2.4}O_7$ NW parallel arrays. (a) Optical image of the leaves covered by the as-fabricated device, while the device area is highlighted by the yellow dashed rectangle. (b) Transmittance measurement of the device. (c) *I*−*V* curves of the device under different power intensities of 261 nm light illumination and in the dark. The inset shows the top-view SEM image of the NW parallel arrayed device channel. (d) Dependence of the photocurrent and the responsivity on the light intensity. The inset gives the device schematic of the photodetector fabricated on glass substrates. (e) Photoresponse characteristics (current *versus* time) of the device. The light intensity is 0.6 mW/cm^2. (f) Corresponding high-resolution current *versus* time curve. The bias is 1 V and V_g = −20 V.

Table 2. Comparison of the Performance Parameters of Transparent Photodetectors Based on InGaZnO NW Arrays among Other Transparent Photodetectors Reported in the Literature

1D photodetector	bias (V)	responsivity/A W^{-1}	photocurrent	rise time/s	decay time/s	ref
ZnO ultraporous film	5	13	1.2 mA	250	150	62
ZnO−SnO_2 nanofibers film	10		7.9 nA	32.2	7.8	63
ZnS-coated ZnO array	3			229	547	64
ITO/ZnO NW/MgO/ITO	5	290				65
ZnO network	1	~10^{-2}	115 μA	3.3	20	66
ITO/ZnO NR/GO:CNT	2	2.4				67
ZnO NW array	5	113		23	73	68
ZnO homojunction nanofibers	0	1	0.5 nA	3.9	4.7	69
vertically aligned ZnO nanostructure	−5	290	0.24 mA		0.22	70
SnO_2−TiO_2 heterojunction core−shell structure	0	0.6	10^{-6} A	0.02	0.004	71
IGZO NW array	−20	64600	5.07 μA	3.67	12.71	this work

responsivity decreases gradually with the increasing incident light power. It gives a maximum responsivity of 1.64 × 10^5 A/W with the source−drain bias of 1 V and gate bias of −20 V. For the photoswitching measurement, the device delivers a stable on- and off-state with an on−off current ratio of ~5, which reveals the stability and reproducibility of the photodetector (Supporting Information Figure S13c). The rise and decay times are determined to be 4.42 and 11.1 s, respectively (Supporting Information Figure S13d). More importantly, the $In_{1.8}Ga_{1.8}Zn_{2.4}O_7$ NW arrays can also be fabricated onto glass substrates with indium tin oxide (ITO) source−drain electrodes in order to achieve fully transparent UV photodetectors (Figure 6). The device schematic and the corresponding top-view SEM image of the NW parallel arrays are given in Figure 6c and d insets, respectively. As shown in the optical image of fabricated transparent photodetectors in Figure 6a, it is evident

DOI: 10.1021/acsnano.9b06311
ACS Nano 2019, 13, 12042−12051

that the underneath leaves can be seen clearly, while the device area is highlighted by the yellow dashed rectangle. The photodetector has a high optical transparency, above 80%, for a wide range of wavelengths spanning from 400 to 800 nm (Figure 6b). When compared with the $I-V$ curves of using Si substrates (Supporting Information Figure S13a), the transparent device also gives a linear $I-V$ characteristic (*i.e.*, ohmic-like contact property), but with a much smaller output current of only 5.1 μA under the same device geometry and bias condition. This reduced current may come from the nonoptimized contact between the NW arrays and the ITO electrodes. Similarly, the sublinear relationship between the photocurrent and the incident light intensity is as well witnessed; however, the responsivity delivers a slightly smaller value of 6.46×10^4 A/W (Figure 6d). In any case, the device exhibits an excellent stability and reproducibility (Figure 6e) with a rise time of 3.67 s and decay time of 12.71 s (Figure 6f). All these performance parameters of the fully transparent photodetector device are already comparable to or even better than those of state-of-the-art transparent photodetectors as reported in the literature (Table 2). All these findings apparently indicate the technological potential of InGaZnO superlattice NW arrays for future high-performance transparent optoelectronics.

CONCLUSIONS

In summary, InGaZnO NWs with controllable stoichiometry and perfect superlattice structure are fabricated by an ambient-pressure chemical vapor deposition (CVD) method. By configuring them into photodetectors, the photoconducting property of InGaZnO and InZnO NWs toward UV irradiation can be thoroughly studied. It is observed that the Ga concentration has a significant effect on the device performance. The introduction of Ga can substantially reduce the amount of oxygen vacancies within NWs because of the higher bonding energy of Ga−O. Therefore, the free carrier generation is restrained, which leads to the reduction of O_2^- adsorption and subsequently improves the photodetector performance. More importantly, when large-scale NW parallel arrays are constructed onto glass substrates, high-performance transparent UV photodetectors can be achieved, suggesting the promising potency of InGaZnO superlattice NW arrays for next-generation fully transparent optoelectronics.

METHODS

Material Synthesis. Both InGaZnO and InZnO (control sample) NWs were fabricated *via* the ambient-pressure CVD method. In detail, Si covered with a 50 nm of SiO_2 was used as the substrate. A thin gold film with a nominal thickness of 0.1 nm was deposited on the surface of the substrate by thermal evaporation serving as the catalysts. To fabricate InGaZnO NWs, the source consists of zinc powder (0.0022 g; >99.8%; Sigma-Aldrich), In granules (0.38 g; 99.999%; China Rare Metal), Ga granules (variation from 0.023 to 0.115 g; 99.999%; China Rare Metal), and graphite powder (0.3 g; Sigma-Aldrich). The source is stable at the closed end of a quartz tube with a length of 10 cm and diameter of 1 cm. There was a distance of 2 cm between the source and the substrate. Next, this small tube was placed inside of a larger quartz tube with a diameter of 1 in.; then this setup was fixed inside of the single-zone horizontal tube furnace. In order to start the growth, the furnace was first increased to the temperature of 990 °C in 20 min; then the system was stabilized at this temperature around 7 min. The gas mixture (oxygen/argon = 1/9; 20 sccm) and argon (99.9995%; 80 sccm) were used as the carrier gas in this experiment. The process was then repeated for another two times (the second growth for 7 min, while 10 min for the third growth) by using the clean substrates and the source from the first growth after the system reached room temperature. As shown in Supporting Information Figure S1, for the first growth, ZnO NWs was fabricated, while $In_{0.015}Zn_{0.985}O$ NWs were obtained by the second growth. For the third growth, InGaZnO NWs could be obtained controllably. InGaZnO NWs with different Ga concentration can reliably be obtained by simply varying the Ga content in the precursor source.

Material Characterization. The crystal structure of the NWs was determined by XRD (D2 Phaser, Bruker). The morphology of the NWs was examined by a scanning electron microscope (Quanta 450 FEG, FEI) and transmission electron microscope (CM 20). The crystallinity of the NWs was also evaluated by HRTEM (JEOL-2001F, JEOL) and SAED. Elemental mappings were performed using EDS.

Fabrication and Measurement of Photodetectors. The obtained NWs were first dispersed in anhydrous 2-propanol solution by ultrasonication followed by transfer onto the surface of p-type Si substrates with a 50-nm-thick thermally grown oxide layer using drop-casting. Next, photolithography was carried out followed by deposition of the Ni film (80 nm) *via* electron beam evaporation and then a lift-off process for the individual NW photodetector. For the transparent NW parallel arrayed photodetectors, the glass substrates predeposited with ITO (60 nm) and Al_2O_3 (100 nm) by sputter and electron-beam evaporation, respectively, were employed as the device substrates. Using NW contact printing, NW parallel arrays could then be easily configured onto the processed substrate. ITO films were used as the source−drain electrodes. Last, all photodetector measurements were performed by using a standard probe station with an Agilent 4155C semiconductor analyzer (Agilent Technologies, Santa Clara, CA, USA) coupled with a 261 nm laser as the light source whose power was measured by a power meter (PM400, Thorlabs).

ASSOCIATED CONTENT

Supporting Information

The Supporting Information is available free of charge on the ACS Publications website at DOI: 10.1021/acsnano.9b06311.

EDS spectra; XRD spectra; repeated growth trial of five times; HRTEM; FFT; EDS mappings; photodetecting performance in ambient and vacuum environment; XPS spectra; variation of the peak area ratio of O 1s for all InGaZnO NW samples (PDF)

AUTHOR INFORMATION

Corresponding Author

*E-mail: johnnyho@cityu.edu.hk.

ORCID

Changyong Lan: 0000-0002-5654-1098

Johnny C. Ho: 0000-0003-3000-8794

Notes

The authors declare no competing financial interest.

ACKNOWLEDGMENTS

This work is financially supported by the National Natural Science Foundation of China (Grants 51672229), the General Research Fund (CityU 11213115), the Theme-based Research (T42-103/16-N) of the Research Grants Council of Hong Kong SAR, China, the Science Technology and Innovation Committee of Shenzhen Municipality (Grant JCYJ20170818-095520778), the Natural Science Foundation of Shandong Province, China (ZR2018JL021), and a grant from the Shenzhen Research Institute, City University of Hong Kong.

DOI: 10.1021/acsnano.9b06311
ACS Nano 2019, 13, 12042−12051

REFERENCES

(1) Lupan, O.; Postica, V.; Wolff, N.; Polonskyi, O.; Duppel, V.; Kaidas, V.; Lazari, E.; Ababii, N.; Faupel, F.; Kienle, L.; Adelung, R. Localized Synthesis of Iron Oxide Nanowires and Fabrication of High Performance Nanosensors Based on a Single Fe_2O_3 Nanowire. *Small* **2017**, *13*, 1602868.

(2) Lupan, O.; Schütt, F.; Postica, V.; Smazna, D.; Mishra, Y. K.; Adelung, R. Sensing Performances of Pure and Hybridized Carbon Nanotubes-ZnO Nanowire Networks: A Detailed Study. *Sci. Rep.* **2017**, *7*, 14715.

(3) Kind, H.; Yan, H.; Messer, B.; Law, M.; Yang, P. Nanowire Ultraviolet Photodetectors and Optical Switches. *Adv. Mater.* **2002**, *14*, 158−160.

(4) Sun, B.; Sun, Y.; Wang, C. Flexible Transparent and Free-Standing SiC Nanowires Fabric: Stretchable UV Absorber and Fast-Response UV-A Detector. *Small* **2018**, *14*, 1703391.

(5) Kent, T. F.; Carnevale, S. D.; Sarwar, A. T. M.; Phillips, P. J.; Klie, R. F.; Myers, R. C. Deep Ultraviolet Emitting Polarization Induced Nanowire Light Emitting Diodes with $Al_xGa_{1-x}N$ Active Regions. *Nanotechnology* **2014**, *25*, 455201.

(6) Chen, W.; Roca i Cabarrocas, P. Rational Design of Nanowire Solar Cells: from Single Nanowire to NanowireArrays. *Nanotechnology* **2019**, *30*, 194002.

(7) Tian, W.; Zhi, C.; Zhai, T.; Chen, S.; Wang, X.; Liao, M.; Golberg, D.; Bando, Y. In-Doped Ga_2O_3Nanobelt Based Photodetector with High Sensitivity and Wide-Range Photoresponse. *J. Mater. Chem.* **2012**, *22*, 17984−17991.

(8) Chen, K. J.; Hung, F. Y.; Chang, S. J.; Young, S. J. Optoelectronic Characteristics of UV Photodetector Based on ZnO Nanowire Thin Films. *J. Alloys Compd.* **2009**, *479*, 674−677.

(9) Cai, G.; Chen, Z.; Qiang, L.; Yan, B.; Zhuo, Y.; Lin, J.; Wang, X.; Pei, Y.; Wang, G. Visible-Blind UV Detector Based on Water-Gated Thin Film Transistor with In_2O_3Channel Grown by Metal-Organic Chemical Vapor Deposition. *Jpn. J. Appl. Phys.* **2018**, *57*, 110301.

(10) Du, J.; Xing, J.; Ge, C.; Liu, H.; Liu, P.; Hao, H.; Dong, J.; Zheng, Z.; Gao, H. Highly Sensitive and Ultrafast Deep UV Photodetector Based on aβ-Ga_2O_3Nanowire Network Grown by CVD. *J. Phys. D: Appl. Phys.* **2016**, *49*, 425105.

(11) Lou, Z.; Li, L.; Shen, G. High-Performance Rigid and Flexible Ultraviolet Photodetectors with Single-Crystalline $ZnGa_2O_4$Nanowires. *Nano Res.* **2015**, *8*, 2162−2169.

(12) Zhou, X.; Zhang, Q.; Gan, L.; Li, X.; Li, H.; Zhang, Y.; Golberg, D.; Zhai, T. High—Performance Solar-Blind Deep Ultraviolet Photodetector Based on Individual Single-Crystalline Zn_2GeO_4 Nanowire. *Adv. Funct. Mater.* **2016**, *26*, 704−712.

(13) Huang, R.; Zhang, J.; Wei, F.; Shi, L.; Kong, T.; Cheng, G. Ultrahigh Responsivity of Ternary Sb-Bi-Se Nanowire Photodetectors. *Adv. Funct. Mater.* **2014**, *24*, 3581−3586.

(14) Kim, Y.; Joyce, H. J.; Gao, Q.; Tan, H. H.; Jagadish, C.; Paladugu, M.; Zou, J.; Suvorova, A. A. Influence of Nanowire Density on the Shape and Optical Properties of Ternary InGaAs Nanowires. *Nano Lett.* **2006**, *6*, 599−604.

(15) Chang, S. J.; Hsiao, C. H.; Lan, B. W.; Hung, S. C.; Huang, B. R.; Young, S. J.; Cheng, Y. C.; Chih, S. H. Growth of Ternary ZnCdSe Nanowires and the Fabrication of ZnCdSe Nanowire Photodetectors. *Superlattices Microstruct.* **2010**, *48*, 50−57.

(16) Wang, J.-L.; Lu, Y.-R.; Li, H.-H.; Liu, J.-W.; Yu, S.-H. Large Area Co-Assembly of Nanowires for Flexible Transparent Smart Windows. *J. Am. Chem. Soc.* **2017**, *139*, 9921−9926.

(17) Divochiy, A.; Marsili, F.; Bitauld, D.; Gaggero, A.; Leoni, R.; Mattioli, F.; Korneev, A.; Seleznev, V.; Kaurova, N.; Minaeva, O.; Gol'tsman, G.; Lagoudakis, K. G.; Benkhaoul, M.; Lévy, F.; Fiore, A. Superconducting Nanowire Photon-Number-Resolving Detector at Telecommunication Wavelengths. *Nat. Photonics* **2008**, *2*, 302−306.

(18) Wu, W.; Wen, X.; Wang, Z. L. Taxel-Addressable Matrix of Vertical-Nanowire Piezotronic Transistors for Active and Adaptive Tactile Imaging. *Science* **2013**, *340*, 952.

(19) Ho, M. D.; Ling, Y.; Yap, L. W.; Wang, Y.; Dong, D.; Zhao, Y.; Cheng, W. Percolating Network of Ultrathin Gold Nanowires and Silver Nanowires toward "Invisible" Wearable Sensors for Detecting Emotional Expression and Apexcardiogram. *Adv. Funct. Mater.* **2017**, *27*, 1700845.

(20) Hwang, B.-U.; Lee, J.-H.; Trung, T. Q.; Roh, E.; Kim, D.-I.; Kim, S.-W.; Lee, N.-E. Transparent Stretchable Self-Powered Patchable Sensor Platform with Ultrasensitive Recognition of Human Activities. *ACS Nano* **2015**, *9*, 8801−8810.

(21) Li, D. P.; Wang, G. Z.; Yang, Q. H.; Xie, X. Synthesis and Photoluminescence of $InGaO_3(ZnO)_m$ Nanowires with Perfect Superlattice Structure. *J. Phys. Chem. C* **2009**, *113*, 21512−21515.

(22) Guo, Y.; Bilzen, B. V.; Locquet, J. P.; Seo, J. W. Formation of Crystalline $InGaO_3(ZnO)_n$Nanowires *via* the Solid-Phase Diffusion Process Using a Solution-Based Precursor. *Nanotechnology* **2015**, *26*, 495601.

(23) Li, F.; Yip, S.; Dong, R.; Zhou, Z.; Lan, C.; Liang, X.; Li, D.; Meng, Y.; Kang, X.; Ho, J. C. Crystalline InGaZnO Quaternary Nanowires with Superlattice Structure for High-Performance Thin-Film Transistors. *Nano Res.* **2019**, *12*, 1796−1803.

(24) Park, K.; Lee, J. A.; Im, H. S.; Jung, C. S.; Kim, H. S.; Park, J.; Lee, C.-L. GaP-ZnS Pseudobinary Alloy Nanowires. *Nano Lett.* **2014**, *14*, 5912−5919.

(25) Lou, Z.; Li, L.; Shen, G. $InGaO_3(ZnO)$ Superlattice Nanowires for High-Performance Ultraviolet Photodetectors. *Adv. Electron. Mater.* **2015**, *1*, 1500054.

(26) Hesse, D.; Lee, S. K.; Gösele, U. Microstructure of (104)-Oriented $Bi_{3.25}La_{0.75}Ti_3O_{12}$ and $Bi_{3.54}Nd_{0.46}Ti_3O_{12}$Ferroelectric Thin Films on Multiply Twinned $SrRuO_3$/Pt(111) Electrodes on YSZ(100)-Buffered Si(100). *Phys. Status Solidi A* **2005**, *202*, 2287−2298.

(27) Chaudhuri, A. R.; Fissel, A.; Osten, H. J. Superior Dielectric Properties for Template Assisted Grown (100) Oriented Gd_2O_3Thin Films on Si(100). *Appl. Phys. Lett.* **2014**, *104*, 012906.

(28) Han, N.; Hou, J. J.; Wang, F.; Yip, S.; Yen, Y.-T.; Yang, Z.-x.; Dong, G.; Hung, T.; Chueh, Y.-L.; Ho, J. C. GaAs Nanowires: From Manipulation of Defect Formation to Controllable Electronic Transport Properties. *ACS Nano* **2013**, *7*, 9138−9146.

(29) Yang, Z.-x.; Han, N.; Fang, M.; Lin, H.; Cheung, H.-Y.; Yip, S.; Wang, E.-J.; Hung, T.; Wong, C.-Y.; Ho, J. C. Surfactant-Assisted Chemical Vapour Deposition of High-Performance Small-Diameter GaSb Nanowires. *Nat. Commun.* **2014**, *5*, 5249.

(30) Hou, J. J.; Han, N.; Wang, F.; Xiu, F.; Yip, S.; Hui, A. T.; Hung, T.; Ho, J. C. Synthesis and Characterizations of Ternary InGaAs Nanowires by a Two-Step Growth Method for High-Performance Electronic Devices. *ACS Nano* **2012**, *6*, 3624−3630.

(31) Na, C. W.; Bae, S. Y.; Park, J. Short-Period Superlattice Structure of Sn-Doped $In_2O_3(ZnO)_4$ and $In_2O_3(ZnO)_5$ Nanowires. *J. Phys. Chem. B* **2005**, *109*, 12785−12790.

(32) Wu, L. L.; Liu, F. W.; Chu, Z. Q.; Liang, Y.; Xu, H. Y.; Lu, H. Q.; Zhang, X. T.; Li, Q.; Hark, S. K. High-Yield Synthesis of $In_{2-x}Ga_xO_3(ZnO)_3$Nanobelts with a Planar Superlattice Structure. *CrystEngComm* **2010**, *12*, 2047−2050.

(33) Wu, L.; Li, Q.; Zhang, X.; Zhai, T.; Bando, Y.; Golberg, D. Enhanced Field Emission Performance of Ga-Doped $In_2O_3(ZnO)_3$ Superlattice Nanobelts. *J. Phys. Chem. C* **2011**, *115*, 24564−24568.

(34) Zheng, Z.; Gan, L.; Li, H.; Ma, Y.; Bando, Y.; Golberg, D.; Zhai, T. A Fully Transparent and Flexible Ultraviolet-Visible Photodetector Based on Controlled Electrospun ZnO-CdO Heterojunction Nanofiber Arrays. *Adv. Funct. Mater.* **2015**, *25*, 5885−5894.

(35) Fu, X.-W.; Liao, Z.-M.; Zhou, Y.-B.; Wu, H.-C.; Bie, Y.-Q.; Xu, J.; Yu, D.-P. Graphene/ZnO Nanowire/Graphene Vertical Structure Based Fast-Response Ultraviolet Photodetector. *Appl. Phys. Lett.* **2012**, *100*, 223114.

(36) Li, L.; Auer, E.; Liao, M.; Fang, X.; Zhai, T.; Gautam, U. K.; Lugstein, A.; Koide, Y.; Bando, Y.; Golberg, D. Deep-Ultraviolet Solar-Blind Photoconductivity of Individual Gallium Oxide Nanobelts. *Nanoscale* **2011**, *3*, 1120−1126.

(37) Liu, K.; Sakurai, M.; Liao, M.; Aono, M. Giant Improvement of the Performance of ZnO Nanowire Photodetectors by Au Nanoparticles. *J. Phys. Chem. C* **2010**, *114*, 19835−19839.

DOI: 10.1021/acsnano.9b06311
ACS Nano 2019, 13, 12042−12051

(38) Manekkathodi, A.; Lu, M.-Y.; Wang, C. W.; Chen, L.-J. Direct Growth of Aligned Zinc Oxide Nanorods on Paper Substrates for Low-Cost Flexible Electronics. *Adv. Mater.* **2010**, *22*, 4059−4063.
(39) Jin, C.; Kim, H.; Ryu, H.-Y.; Kim, H. W.; Lee, C. Subwavelength Optical Resonant Cavity-Induced Enhancement of the Near-Band-Edge Emission from ZnO-Core/SnO_2-Shell Nanorods. *J. Phys. Chem. C* **2011**, *115*, 8513−8518.
(40) Ahn, S.-E.; Ji, H. J.; Kim, K.; Kim, G. T.; Bae, C. H.; Park, S. M.; Kim, Y.-K.; Ha, J. S. Origin of the Slow Photoresponse in an Individual Sol-Gel Synthesized ZnO Nanowire. *Appl. Phys. Lett.* **2007**, *90*, 153106.
(41) Kouklin, N. Cu-Doped ZnO Nanowires for Efficient and Multispectral Photodetection Applications. *Adv. Mater.* **2008**, *20*, 2190−2194.
(42) Ate, A.; Zhu, H.; Cai, H.; Quan, X.; Wang, X.; Jia, X.; Zhang, J.; Wang, K.; Jia, X.; Tang, Z. High Performance UV Sensor Based on Individual ZnO Nanowire and Photoelectric Properties of Individual ZnO Nanowire Surface in Different Atmospheres. *AIP Conf. Proc.* **2013**, *1586*, 52−56.
(43) Li, Q. H.; Gao, T.; Wang, Y. G.; Wang, T. H. Adsorption and Desorption of Oxygen Probed from ZnO Nanowire Films by Photocurrent Measurements. *Appl. Phys. Lett.* **2005**, *86*, 123117.
(44) Zhou, J.; Gu, Y.; Hu, Y.; Mai, W.; Yeh, P.-H.; Bao, G.; Sood, A. K.; Polla, D. L.; Wang, Z. L. Gigantic Enhancement in Response and Reset Time of ZnO UV Nanosensor by Utilizing Schottky Contact and Surface Functionalization. *Appl. Phys. Lett.* **2009**, *94*, 191103.
(45) Park, G. C.; Hwang, S. M.; Choi, J. H.; Kwon, Y. H.; Cho, H. K.; Kim, S.-W.; Lim, J. H.; Joo, J. Effects of In or Ga Doping on the Growth Behavior and Optical Properties of ZnO Nanorods Fabricated by Hydrothermal Process. *Phys. Status Solidi A* **2013**, *210*, 1552−1556.
(46) Pan, X.; Yang, M.-Q.; Fu, X.; Zhang, N.; Xu, Y.-J. Defective TiO_2 with Oxygen Vacancies: Synthesis, Properties and Photocatalytic Applications. *Nanoscale* **2013**, *5*, 3601−3614.
(47) Guo, D. Y.; Wu, Z. P.; An, Y. H.; Guo, X. C.; Chu, X. L.; Sun, C. L.; Li, L. H.; Li, P. G.; Tang, W. H. Oxygen Vacancy Tuned Ohmic-Schottky Conversion for Enhanced Performance in β-Ga_2O_3Solar-Blind Ultraviolet Photodetectors. *Appl. Phys. Lett.* **2014**, *105*, 023507.
(48) Li, Y.; Valle, F. D.; Simonnet, M.; Yamada, I.; Delaunay, J.-J. Competitive Surface Effects of Oxygen and Water on UV Photoresponse of ZnO Nanowires. *Appl. Phys. Lett.* **2009**, *94*, 023110.
(49) Li, D.; Lan, C.; Manikandan, A.; Yip, S.; Zhou, Z.; Liang, X.; Shu, L.; Chueh, Y.-L.; Han, N.; Ho, J. C. Ultra-Fast Photodetectors Based on High-Mobility Indium Gallium Antimonide Nanowires. *Nat. Commun.* **2019**, *10*, 1664.
(50) Rao, C. N. R.; Kulkarni, G. U.; Thomas, P. J.; Edwards, P. P. Size-Dependent Chemistry: Properties of Nanocrystals. *Chem. - Eur. J.* **2002**, *8*, 28−35.
(51) Volokitin, Y.; Sinzig, J.; de Jongh, L. J.; Schmid, G.; Vargaftik, M. N.; Moiseevi, I. I. Quantum-Size Effects in the Thermodynamic Properties of Metallic Nanoparticles. *Nature* **1996**, *384*, 621−623.
(52) Rim, Y. S.; Kim, D. L.; Jeong, W. H.; Kim, H. J. Effect of Zr Addition on ZnSnO Thin-Film Transistors using a Solution Process. *Appl. Phys. Lett.* **2010**, *97*, 233502.
(53) Kamiya, T.; Hosono, H. Material Characteristics and Applications of Transparent Amorphous Oxide Semiconductors. *NPG Asia Mater.* **2010**, *2*, 15.
(54) Jeong, S.; Ha, Y.-G.; Moon, J.; Facchetti, A.; Marks, T. J. Role of Gallium Doping in Dramatically Lowering Amorphous-Oxide Processing Temperatures for Solution-Derived Indium Zinc Oxide Thin-Film Transistors. *Adv. Mater.* **2010**, *22*, 1346−1350.
(55) Zhou, Z.; Lan, C.; Yip, S.; Wei, R.; Li, D.; Shu, L.; Ho, J. C. Towards High-Mobility $In_{2x}Ga_{2-2x}O_3$Nanowire Field-Effect Transistors. *Nano Res.* **2018**, *11*, 5935−5945.
(56) Shinde, S. S.; Rajpure, K. Y. Fast Response Ultraviolet Ga-Doped ZnO Based Photoconductive Detector. *Mater. Res. Bull.* **2011**, *46*, 1734−1737.
(57) Keem, K.; Kim, H.; Kim, G.-T.; Lee, J. S.; Min, B.; Cho, K.; Sung, M.-Y.; Kim, S. Photocurrent in ZnO Nanowires Grown from Au Electrodes. *Appl. Phys. Lett.* **2004**, *84*, 4376−4378.
(58) Lei, B.; Li, C.; Zhang, D.; Tang, T.; Zhou, C. Tuning Electronic Properties of In_2O_3Nanowires by DopingControl. *Appl. Phys. A: Mater. Sci. Process.* **2004**, *79*, 439−442.
(59) Zou, X.; Liu, X.; Wang, C.; Jiang, Y.; Wang, Y.; Xiao, X.; Ho, J. C.; Li, J.; Jiang, C.; Xiong, Q.; Liao, L. Controllable Electrical Properties of Metal-Doped In_2O_3 Nanowires for High-Performance Enhancement-Mode Transistors. *ACS Nano* **2013**, *7*, 804−810.
(60) Han, N.; Yang, Z.; Wang, F.; Yip, S.; Dong, G.; Liang, X.; Hung, T.; Chen, Y.; Ho, J. C. Modulating the Morphology and Electrical Properties of GaAs Nanowires *via* Catalyst Stabilization by Oxygen. *ACS Appl. Mater. Interfaces* **2015**, *7*, 5591−5597.
(61) Han, N.; Yang, Z.-x.; Wang, F.; Yip, S.; Li, D.; Hung, T. F.; Chen, Y.; Ho, J. C. Crystal Orientation Controlled Photovoltaic Properties of Multilayer GaAs Nanowire Arrays. *ACS Nano* **2016**, *10*, 6283−6290.
(62) Nasiri, N.; Bo, R.; Wang, F.; Fu, L.; Tricoli, A. Ultraporous Electron-Depleted ZnO Nanoparticle Networks for Highly Sensitive Portable Visible-Blind UV Photodetectors. *Adv. Mater.* **2015**, *27*, 4336−4343.
(63) Tian, W.; Zhai, T.; Zhang, C.; Li, S.-L.; Wang, X.; Liu, F.; Liu, D.; Cai, X.; Tsukagoshi, K.; Golberg, D.; Bando, Y. Low-Cost Fully Transparent Ultraviolet Photodetectors Based on Electrospun ZnO-SnO_2 Heterojunction Nanofibers. *Adv. Mater.* **2013**, *25*, 4625−4630.
(64) Bera, A.; Basak, D. Photoluminescence and Photoconductivity of ZnS-Coated ZnO Nanowires. *ACS Appl. Mater. Interfaces* **2010**, *2*, 408−412.
(65) Yang, X.; Qiu, Z.; Li, X.; Lu, J.; Cao, B. Performance Improvement of Ultraviolet Sensor of ZnO Nanorod Arrays. *Appl. Phys. Express* **2013**, *6*, 125201.
(66) Kiruthika, S.; Singh, S.; Kulkarni, G. U. Large Area Transparent ZnO Photodetectors with Au Wire Network Electrodes. *RSC Adv.* **2016**, *6*, 44668−44672.
(67) Leung, Y. H.; He, Z. B.; Luo, L. B.; Tsang, C. H. A.; Wong, N. B.; Zhang, W. J.; Lee, S. T. ZnO Nanowires Array *p-n*Homojunction and its Application as a Visible-Blind Ultraviolet Photodetector. *Appl. Phys. Lett.* **2010**, *96*, 053102.
(68) Yin, L.; Ding, H.; Yuan, Z.; Huang, W.; Shuai, C.; Xiong, Z.; Deng, J.; Lv, T. A Simple and Transparent Well-Aligned ZnO Nanowire Array Ultraviolet Photodetector with High Responsivity. *Opt. Mater.* **2018**, *80*, 149−153.
(69) Ning, Y.; Zhang, Z.; Teng, F.; Fang, X. Novel Transparent and Self-Powered UV Photodetector Based on Crossed ZnO Nanofiber Array Homojunction. *Small* **2018**, *14*, 1703754.
(70) Jung, B. O.; Kim, D. C.; Kong, B. H.; Kim, D.-W.; Cho, H. K. Fully Transparent Vertically Aligned ZnO Nanostructure-Based Ultraviolet Photodetectors with High Responsivity. *Sens. Actuators, B* **2011**, *160*, 740−746.
(71) Gao, C.; Li, X.; Zhu, X.; Chen, L.; Wang, Y.; Teng, F.; Zhang, Z.; Duan, H.; Xie, E. High Performance, Self-Powered UV-Photodetector Based on Ultrathin, Transparent, SnO_2-TiO_2Core-Shell Electrodes. *J. Alloys Compd.* **2014**, *616*, 510−515.

DOI: 10.1021/acsnano.9b06311
ACS Nano 2019, 13, 12042−12051